Atmos. Meas. Tech. Discuss., 8, 3423–3469, 2015
www.atmos-meas-tech-discuss.net/8/3423/2015/
doi:10.5194/amtd-8-3423-2015

Atmospheric Measurement Techniques Discussions

The impact of vibrational Raman scattering of air on DOAS measurements of atmospheric trace gases

J. Lampel[1,*], **U. Frieß**[1], **and U. Platt**[1]

[1]Institute of Environmental Physics, University of Heidelberg, Heidelberg, Germany
[*]now at: Max Planck Institute for Chemistry, Mainz, Germany

Received: 29 January 2015 – Accepted: 27 February 2015 – Published: 31 March 2015

Correspondence to: J. Lampel (johannes.lampel@iup.uni-heidelberg.de)

Published by Copernicus Publications on behalf of the European Geosciences Union.

Abstract

In remote sensing applications, such as differential optical absorption spectroscopy (DOAS), atmospheric scattering processes need to be considered. After inelastic scattering on N_2 and O_2 molecules, the scattered photons occur as additional intensity at a different wavelength, effectively leading to filling-in of both solar Fraunhofer lines and absorptions of atmospheric constituents.

Measured spectra in passive DOAS applications are typically corrected for rotational Raman scattering (RRS), also called Ring effect, which represents the main contribution to inelastic scattering. In contrast to that, vibrational Raman scattering (VRS) of N_2 and O_2 has often been thought to be negligible, but also contributes.

Consequences of VRS are red-shifted Fraunhofer structures in scattered light spectra and filling-in of Fraunhofer lines, additional to RRS. We describe how to calculate VRS correction spectra in analogy to the Ring spectrum.

We discuss further the impact of VRS cross-sections for O_2 and N_2 on passive DOAS measurements. The relevance of VRS is shown for the first time in spectral evaluations of Multi-Axis DOAS data. This measurement data yields in agreement with calculated scattering cross-sections, that the observed VRS cross-section amounts to 2.2 ± 0.4 % of the cross-section of RRS under tropospheric conditions. It is concluded, that this phenomenon has to be included in the spectral evaluation of weak absorbers as it reduces the measurement error significantly and can cause apparent differential optical depth of up to 2.5×10^{-4}. Its influence on the spectral retrieval of IO, Glyoxal, water vapour and NO_2 in the blue wavelength range is evaluated. For measurements with a large Ring signal a significant and systematic bias of NO_2 dSCDs up to $(-3.8 \pm 0.4) \times 10^{14}$ molec cm^{-2} at low elevation angles is observed if this effect is not considered.

AMTD
8, 3423–3469, 2015

1 Introduction

The DOAS-technique (Differential Optical Absorption Spectroscopy) (Platt and Stutz, 2008) is widely used from different platforms to retrieve the abundance of tropospheric and stratospheric absorbers, such as O_3, NO_2, OClO, BrO and many others (e.g. Hendrick et al., 2011; Vandaele et al., 2005; Roscoe et al., 2010; Aliwell et al., 2002). Observation geometries include zenith-sky and off-axis measurement of sunlight scattered in the atmosphere (e.g. Platt and Stutz, 2008). The Multi-AXis (MAX)-DOAS principle allows to reach higher sensitivity to tropospheric absorbers, such as e.g. NO_2, IO, BrO, water vapour, Glyoxal and HCHO (e.g. Peters et al., 2012; Großmann et al., 2013; Frieß et al., 2011; Wagner et al., 2013; Mahajan et al., 2014; Pinardi et al., 2013).

Solar absorption lines (Fraunhofer lines) have an effect on the evaluation of scattered sunlight spectra, since inelastic scattering processes in the atmosphere lead to an effective "filling in" of these absorption lines. The reduction of the optical densities (OD) of Fraunhofer lines – in particular of narrow lines – is known as the Ring effect (Grainger and Ring, 1962). While originally several mechanisms for the Ring effect were proposed (Burrows et al., 1996, and references therein) there is a consensus in recent literature that most properties of the Ring effect can be described by rotational Raman scattering (Solomon et al., 1987; Fish and Jones, 1995; Joiner and Bhartia, 1995; Joiner et al., 1995; Burrows et al., 1996; Vountas et al., 1998).

However, for large amounts of filling in of Fraunhofer lines, i.e. a strong Ring signal, Schönhardt et al. (2008) reported problems with the spectral retrieval of IO from satellite measurements at wavelengths above 431 nm. Unexplained residual optical densities were observed, indicating an effect which was not considered in the spectral analysis. We propose that this effect is at least partly due to vibrational Raman scattering (VRS) in the atmosphere. This spectral region (i.e. 430 nm–440 nm) is actually the location of the strong Ca-lines of the Fraunhofer spectrum, red-shifted by the excitation energy of the first vibrational eigenstate of N_2.

AMTD
8, 3423–3469, 2015

This is a first indication that this effect might indeed be relevant for measurements of atmospheric absorbers. Additionally, Coburn et al. (2011) reported that despite co-adding of measurement spectra, the size of the residual spectral structures from MAX-DOAS observations in the blue wavelength range did not reduce as expected from photon statistics. They suggested that an insufficiently modelled Ring-spectrum or a missing contribution such as vibrational Raman scattering is causing this difference. In spectral retrievals of trace gases encompassing the wavelength range between 430–440 nm, this effect is currently not explicitly considered.

Figure 1 shows the cross-section of rotational and vibrational Raman scattering for forward scattering of a monochromatic light beam at 393 nm (the position of the solar Calcium-II K-absorption line). While the pure rotational Raman lines of N_2 or O_2 appear in the vicinity of the wavelength region of 393 nm, the rotational-vibrational Raman (Stokes) lines of N_2 and O_2 are considerably red-shifted according to their different vibrational constants. VRS of O_2 leads to a red-shift of the Calcium-II K-absorption line of 25 nm, VRS of N_2 to 40 nm. (Note that anti-Stokes lines are very weak under atmospheric conditions, since only a small fraction of the N_2 and O_2 molecules is vibrationally excited.) The rotational constant and vibrational constants are listed in Table 1. Thus, strong Fraunhofer lines can give rise to VRS – "ghost" absorption lines in other parts of the spectrum.

In addition, also water vapour exhibits narrow vibrational Raman transitions, with a frequency shift of around 3654 cm^{-1} (Penney et al., 1974; Murphy, 1978) and with a cross-section of $8(\pm 20\,\%) \times 10^{-30}$ $cm^2\,sr^{-1}$ (Rizi et al., 2004) about 5–10 times as strong as the vibrational Raman scattering cross-section of the $\Delta\nu = 1$ transition of N_2 (depending on the scattering angle). This effectively leads to a wavelength shift of the Ca-Fraunhofer lines to about 460 nm, but this should usually not be observable in current DOAS measurements since the expected OD would be below 5×10^{-5} for a typical tropospheric water vapour column density of 5×10^{23} molec cm^{-2} along a light path of 10 km. Inelastic scattering of air and water vapour is however used in LIDAR applications (Weitkamp, 2005).

AMTD
8, 3423–3469, 2015

In the atmosphere, not only monochromatic light is scattered by air molecules, but rather a continuous incident light spectrum from the Sun. The solar spectrum is highly structured by Fraunhofer lines. These spectral structures are red-shifted by VRS and will result in so called "Fraunhofer ghosts" in another spectral interval. If this additional intensity is not explicitly corrected for, it can lead to errors in the retrieved trace gas concentrations. Intensities of elastically and inelastically scattered sunlight are shown in Fig. 2, together with a constant offset (e.g. caused by instrumental stray light) and vibrational Raman scattering in liquid water (Vountas et al., 2003; Dinter et al., 2015).

Platt et al. (1997) mentioned that VRS of air can lead to apparent ODs of up to 0.3 % in zenith sky measurements. Vountas et al. (1998) estimated the effect of single vibrational Raman scattering to the filling-in of Fraunhofer lines to be less than 0.3 % and did not discuss it further. Haug (1996) and Platt and Stutz (2008) estimated the filling-in to be 0.02–0.22 %, which results in 2–14 % of the filling-in due to rotational Raman scattering. However, none of these publications showed experimental evidence from DOAS measurements to support their estimates.

When the scattering medium does not exhibit narrow excitation states, this can lead to a "blurred" remapping of the solar spectrum. This is the case for some liquids and solids. Vibrational Raman scattering in liquid water has been reported by Vountas et al. (2003). Similar to ice, liquid water has a broad Raman spectrum (Raman shift of $\approx 3300\,\mathrm{cm}^{-1}$ with a FWHM of $\approx 500\,\mathrm{cm}^{-1}$, which converts to a shift of ≈ 61 nm at $\lambda = 400$ nm and a FWHM of ≈ 11 nm at $\lambda' = 461$ nm, according to Haltrin and Kattawar, 1993) and thus essentially creates an intensity offset in measurement spectra. Therefore, the VRS(liq. H2O) correction spectrum for this effect is similar to the offset polynomial often used in DOAS evaluations to compensate for intensity offsets caused by instrumental stray-light, but has a broad-band (10 nm) modulation of its amplitude.

In contrast to that, the Raman spectra of N_2 and O_2 contain individual and narrow peaks, therefore resulting in narrow-band contributions to the total measured OD. These can also affect the spectral retrieval of trace gases, if vibrational Raman "ghosts"

AMTD
8, 3423–3469, 2015

of strong Fraunhofer lines happen to occur in a spectral region which is relevant for the spectral retrieval.

The additional intensity offset, which is included in several settings for DOAS evaluations of stray-light spectra is typically meant to compensate for a constant contribution to the measured intensity due to instrumental stray-light. As it turns out, this correction term also compensates for a large fraction of the contribution of vibrational Raman scattering in the atmosphere, especially involving transitions due to vibrational rotational Raman scattering (VRRS).

2 Quantitative description of rotational- and vibrational-Raman scattering by N_2 and O_2

The scattered power density $I_{v,J\to v',J'}$ in $\mathrm{W\,m^{-2}}$ scattered into the full solid angle 4π involving a transition $(v, J \to v', J')$ is given e.g. by Long (2002):

$$I_{v,J\to v',J'} = I_0 \sigma_{v,J\to v',J'} L N g_J (2J+1) \frac{1}{Z} e^{-E(v,J)/kT} \quad (1)$$

where I_0 is the incident power density, N the number density of molecules in the scattering volume, L the length of the scattering volume (i.e. its extent in the direction of the line of sight of the instrument) and g_J is the statistical weight factor of the initial rotational state due to the nuclear spin (see Table 2).

J is the rotational quantum number for the shell angular momentum. v is the vibrational quantum number of the respective molecule. Where J and v describe the intial state, J' and v' describe the final state, respectively. To avoid confusion the vibrational constant of a molecule in units of wavenumbers is denoted $\widetilde{\nu}$. The factor $(2J+1)$ accounts for the degeneracy due to the magnetic quantum numbers while $\exp(-E(v,J)/kT)$ accounts for the population of the initial state of the molecule at temperature T. The absolute cross-section in Eq. (1) is given by $\sigma_{v,J\to v',J'}$ which can be

AMTD
8, 3423–3469, 2015

obtained by integration of the differential cross-section $\frac{d\sigma(\Theta)_{v,J\to v',J'}}{d\Omega}$ (see Eq. 6) over the entire solid angle (note that the term *differential* refers here to the solid angle).

The sum over states (or partitioning function) $Z = Z_{rot}Z_{vib}$ is given by the product of the rotational state sum Z_{rot} and the vibrational state sum Z_{vib}:

$$Z_{rot} = \sum_{J}^{\infty} g_J(2J+1)e^{-E_{rot}(J)/kT} \tag{2}$$

$$Z_{vib} = \sum_{v}^{\infty} e^{-E_{vib}(v)/kT} \tag{3}$$

Z_{vib} can be calculated explicitly using a geometric series:

$$Z_{vib} = \frac{e^{-\frac{hc\tilde{\nu}}{2kT}}}{1-e^{-\frac{hc\tilde{\nu}}{kT}}} \tag{4}$$

The energy of the molecule is characterized by the vibrational (v) and rotational (J) quantum numbers and given by

$$\begin{aligned} E(v,J) &= E_{rot} + E_{vib} \\ &= hcBJ(J+1) + hc\tilde{\nu}\left(v+\frac{1}{2}\right) \end{aligned} \tag{5}$$

assuming no coupling between rotation and vibration, which is a reasonable approximation for typical spectral resolutions used in DOAS applications. B is the rotational constant in wavenumbers and $\tilde{\nu}$ is the wavenumber in cm^{-1} corresponding to the energy difference between the vibrational states (compare Table 1). Allowed transitions are denoted by $\Delta J = 0, \pm 2$ resulting in the Q ($\Delta J = 0$), O ($\Delta J = -2$) and S branches ($\Delta J = 2$) and $\Delta v = 1$ for vibrational transitions. As noted above, due to the temperatures in the Earth's atmosphere only the ground vibrational state is occupied significantly, thus leading only to Stokes-transitions of the vibrational states. ($E_{vib}/kT \approx 11$ and 8 for N_2 and O_2, respectively.)

AMTD
8, 3423–3469, 2015

The differential cross-section for an incident light beam with the wavenumber $\widetilde{\nu}_{\mathrm{in}}$ in cm^{-1} can be written as:

$$\frac{\mathrm{d}\sigma(\Theta)_{v,J\to v',J'}}{\mathrm{d}\Omega} = 8\pi^4(\widetilde{\nu}_{\mathrm{in}} + \widetilde{\nu}_{v,J\to v',J'})^4 \frac{1}{2J+1} \sum_{M,M'} \sum_{ij} [\alpha_{ij}^2]_{(v,J,M\to v',J',M')} f_{ij}(\Theta) \tag{6}$$

where α_{ij} are the entries of the polarisability tensor as given by Long (2002). These can be spatially averaged over the magnetic quantum numbers M, M' since the molecules' orientations in space are arbitrary, which results in the spatially averaged squares of the polarization tensor entries, $\overline{\alpha_{ij}^2}$, see Table 4, which is given by:

$$\overline{[\alpha_{ij}^2]_{(v,J\to v',J')}} = \frac{1}{2J+1} \sum_{M,M'} [\alpha_{ij}^2]_{(v,J,M\to v',J',M')} \tag{7}$$

The invariants of this tensor are the average polarisability a and the anisotropy γ and a' and γ'', their derivatives with respect to nuclear coordinates for vibrational-rotational transitions, respectively. Their contributions to the cross-section corresponding to different transitions are listed in Table 4. The wavelength dependence of a, a', γ and γ' is small (for γ less than 5 % variation for wavelengths from 400–500 nm, see e.g. Bates, 1984) and is therefore neglected here.

The Placzek–Teller coefficients $b_{J,J'}$ used in Table 4 can be e.g. found at Penney et al. (1974):

$$b_{J\to J} = \frac{J(J+1)}{(2J-1)(2J+3)} \tag{8}$$

$$b_{J\to J+2} = \frac{3(J+1)(J+2)}{2(2J+1)(2J+3)} \tag{9}$$

$$b_{J\to J-2} = \frac{3J(J-1)}{2(2J+1)(2J-1)} \tag{10}$$

AMTD
8, 3423–3469, 2015

The geometric factors $f_{ij}(\Theta)$ in Eq. (6) are determined by the relative orientations of the incident light polarisation, the polarisability tensor and the direction of observation, given by the scattering angle Θ. Using Table 4 the non-normalized phase function $p'(\Theta)$ for each of the scattering processes can be calculated. $p'(\Theta)^{\mathrm{VRS}}$ depends thus also on the ratio of $b'^2 = \frac{\gamma'^2}{a'^2}$ and shows more dominant scattering into the forward and backward direction and differs for N_2 and O_2, compare Table 3.

$$p'(\Theta)^{\mathrm{RRS}} = p'(\Theta)^{\mathrm{VRRS}} = 13 + \cos^2(\Theta) \tag{11}$$

$$p'(\Theta)^{\mathrm{VRS}} = \left(1 + \frac{7}{45}b'^2\right) + \left(1 + \frac{3}{45}b'^2\right) \cdot \cos^2(\Theta) \tag{12}$$

From the general expression for the total cross-section

$$\sigma^{\mathrm{total}} = \sum_{v,J} \sigma_{v,J \to v',J'} \frac{1}{Z} g_J (2J+1) e^{-E(v,J)/kT} \tag{13}$$

the total cross-section of the Q branch of the vibrational transition can now be calculated (e.g. Schrötter and Klöckner, 1979) by summing over all possible transitions ($\Delta J = 0; \Delta v = 1$):

$$\sigma^{Q,\mathrm{total}} = \frac{128\pi^5(\widetilde{\nu}_{\mathrm{in}} + \widetilde{\nu})^4}{9(1 - e^{-hc\widetilde{\nu}/kT})} \left[3a'^2 + \frac{2}{3}\gamma'^2 S_{\Delta J=0}\right] \frac{h}{8c\pi^2\widetilde{\nu}} \tag{14}$$

using

$$S_{\Delta J=0} = \sum_J \frac{1}{Z_{\mathrm{rot}}} g_J (2J+1) b_{J,J} e^{-E_{\mathrm{rot}}(J)/kT} \tag{15}$$

$\sigma^{Q,\mathrm{total}}$ depends only slightly on the temperature, since also $S_{\Delta J=0}$ varies by less than 1 % between $T = 230$ K and $T = 298$ K and the term $1 - e^{-hc\widetilde{\nu}/kT}$ less than 10^{-4}.

AMTD
8, 3423–3469, 2015

The numerical values for the resulting overall cross-section are given in Table 6.

The important information for passive DOAS applications is the $(\widetilde{\nu}_{\mathrm{in}}+\widetilde{\nu})^4$-dependency from Eq. (14), together with the spectral shift $\widetilde{\nu}$ (Table 1) itself. This information already allows the calculation of correction spectra in a first approximation. The remaining calculations are necessary to obtain the absolute magnitude of the effect. The resulting apparent optical densities are shown in Fig. 3.

3 Experimental method

The DOAS method (Platt and Stutz, 2008) relies on attenuation of light from different light sources by absorbers within the light path according to Lambert-Beer's law. Calculating the optical density (OD)

$$\tau(\lambda) = -\ln\frac{I(\lambda)}{I_0(\lambda)} \tag{16}$$

from two spectra $I(\lambda)$ and $I_0(\lambda)$ can be used to reconstruct this OD by different absorbers in the respective wavelength range. To remove broad band Mie and Rayleigh extinction, the OD is subdivided in a narrow-band (differential) and a broad-band part, $\tau = \tau_{\mathrm{B}} + \tau_{\mathrm{d}}$. τ_{d} can then be expressed by a sum of the differential parts of possible absorbers with their differential absorption cross-sections $\sigma_{\mathrm{d},i}$. c_i are the respective concentrations along the light path L.

$$\tau_{\mathrm{d}} = \sum_i L c_i \sigma_{\mathrm{d},i} \tag{17}$$

The method of Multi-Axis DOAS (MAX-DOAS) measurements was first described by Hönninger and Platt (2002) and uses scattered sunlight at different elevation angles, which have each a different sensitivity for absorptions in different heights in the atmosphere. Low elevation angles have a higher sensitivity to absorbers close to the

AMTD
8, 3423–3469, 2015

surface, because the difference in the corresponding light path compared to a reference spectrum is mostly located within the lowermost layers of the atmosphere.

Differential slant column densities (dSCDs) S_i can be calculated from MAX-DOAS measurements for each fitted trace gas: a Fraunhofer reference spectrum I_0 is chosen and the dSCD $\Delta S(\alpha) = S(\alpha) - S_{\text{ref}}$ is obtained from the DOAS fit of the OD for each elevation angle α. The SCD is defined by the integral over the concentration c_i along the light path L and is hence given in the unit molec cm^{-2}.

3.1 Instrumentation

The MAX-DOAS measurement data used here was recorded during research cruise M91 of the German research vessel *Meteor* in the Peruvian Upwelling (Bange, 2013). The cruise was part of the "Surface Ocean Processes in the Anthropocene" (SOPRAN)-project as part of SOLAS. The ship left Callao (12°2′30″ S, 77°8′36″ W), the harbor of Lima, on 1 December 2012. It then sailed north until 5° S and continued south along transects perpendicular to the coastline until 18° S and arrived again in Lima on 26 December 2012. A cruise track is shown in Fig. 4.

The MAX-DOAS instrument consisted of three main parts: a telescope unit mounted on top of the air chemistry lab on RV *Meteor* headed towards port side in a height of approximately 28 m, a temperature stabilized Acton spectrometer located inside the lab and a PC to control the devices. The same setup was used by Großmann et al. (2013).

The telescope unit has an inclinometer to correct the ships roll angle for elevation angles close to the horizon. Its output is directly fed into the motor controller and can correct the elevation angle at an accuracy of $\approx 0.5°$ while the ship's roll is less than 8°, which was the case most of the time. The light from the telescope is focused via a lens onto 37 circularly arranged fibres of 100 µm diameter. These fibres are then again used as the entrance slit of the spectrometer. To avoid the influence of direct sunlight reflected in the entrance of the telescope, a 5 cm long baffle was attached.

The spectrometer used was an Acton 300i which was temperature stabilized at 44 °C with an Andor CCD Camera "DU 440-BU". The camera was used in imaging mode

AMTD
8, 3423–3469, 2015

recording 256 × 2048 pixel. The detector of the camera was cooled to −30 °C to reduce the dark-current signal. This setup covered a wavelength range from 324 nm to 467 nm. The full-width-half-maximum resolution was 0.45 nm or 6.5 pixel.

During daylight, spectra were recorded for one minute each at elevation angles of 90° (zenith), 40, 20, 10, 6, 4, 2, 1°, respectively, as long as solar zenith angles (SZA) were ≤ 85°. During twilight (85° ≤ SZA ≤ 105°) spectra were alternatingly recorded at 90 and 2° elevation. At night (SZA ≥ 110°) dark current and offset spectra were recorded automatically. Mercury discharge lamp spectra to obtain the instrument function $H(\lambda, \lambda')$ were recorded manually.

3.2 Spectral retrieval

The recorded scattered sunlight spectra were analyzed for absorptions using the software package DOASIS (Kraus, 2006). A Fraunhofer reference spectrum (FRS) I_0 from the current elevation sequence at an elevation angle of 40° was chosen. The measured OD τ_{Obs} was then calculated for each spectrum I:

$$\tau_{\text{Obs}} = -\ln\left(\frac{I}{I_0}\right) \tag{18}$$

In order to reduce noise, several elevation sequences were co-added. When adding 16 elevation sequences (corresponding to two hours measurement time), a mean RMS of the residual of 7.5×10^{-5} is observed. An example fit is shown in Fig. 5. Adding more than 16 elevation sequences is typically not possible due to instrumental instabilities and changing atmospheric conditions and radiative transfer.

The pixel to wavelength mapping for the recorded spectra was performed by using mercury emission lines. The correctness of the pixel to wavelength mapping was tested by convoluting a high-resolution sunlight spectrum by Chance and Kurucz (2010) and comparing it to a measured spectrum.

The (rotational) Ring spectrum was taken from DOASIS where it is calculated according to Bussemer (1993) for each reference spectrum, agreeing with the expression

AMTD
8, 3423–3469, 2015

given in Eq. (1), without vibrational transitions. A second Ring spectrum, the original one scaled by $\lambda^4/\lambda_0^4 - 1$ to account for radiative transfer effects discussed in Wagner et al. (2009) was also included in the fit and was clearly detected in the measured OD.

The cross-sections listed in Table 5 were used after being convoluted with the instrument function. The instrument function was measured as the response of the spectrometer to the mercury emission line at 404.656 nm.

It was not necessary to incorporate tropospheric ozone absorption cross-sections in the fit, since the expected OD due to stratospheric ozone is $\tau \leq 1 \times 10^{-4}$. However, the resulting stratospheric light path change during morning and evening made it necessary to include an ozone cross-section measured at 223 K by Serdyuchenko et al. (2014). The zeroth order intensity offset correction was realized by including an inverse reference spectrum in the DOAS fit.

For water vapour absorptions based on HITEMP (Rothman et al., 2013), the relative sizes of the absorption bands in the fit interval were adjusted according to Lampel et al. (2015). This correction was not crucial for the detection of VRS, but yields reasonable water vapour dSCDs even for the weak water vapour absorption band at 426 nm.

The effect of vibrational Raman scattering in liquid water on the spectral retrieval of IO has been discussed in greater detail in Peters et al. (2014) and Großmann et al. (2013) using a spectrum based on Vountas et al. (2003). This correction spectrum was not used here, since it was not clearly identified for positive elevation angles. If there was any contribution, it is most likely compensated to a large extend by the additional intensity polynomial within this relatively small wavelength interval as discussed in Richter et al. (2011).

Despite previously reported significant absorption of glyoxal in the eastern Pacific region by Sinreich et al. (2010), no absorption of glyoxal during the cruise was found to exceed our detection limit of $2\sigma = 5 \times 10^{14}$ molec cm^{-2} at low elevation angles of 1–3° in the wavelength interval from 432–460 nm. This is in agreement with other observations listed in Mahajan et al. (2014). The absorption of the oxygen dimer O_4 was additionally included in the DOAS evaluation. Sensitivity studies were performed using the litera-

AMTD
8, 3423–3469, 2015

ture cross-sections published by Hermans et al. (1999); Greenblatt et al. (1990) and Thalman and Volkamer (2013). The average observed glyoxal dSCD was found between $(1–2 \pm 3) \times 10^{14}$ molec cm^{-2}, resulting in surface concentrations of (10 ± 15) ppt. In the wavelength interval used here from 418–438 nm this upper limits corresponds to an OD of glyoxal of less than 10^{-4}. Consequently, the glyoxal cross-section was not included in the final DOAS analysis.

While for the Ring spectrum neither shift nor squeeze was allowed, the remaining cross-sections' shift and squeeze parameter were linked together and determined by fitting the measurement spectrum against the *Kitt Peak Flux Atlas 2010* by Chance and Kurucz (2010). No significant differences were found when determining shift and squeeze of all cross-sections together using the Levenberg Marquard implementation of the DOAS-fit within DOASIS.

According to Eq. (1) the intensity correction spectra for vibrational Raman scattering can be calculated, either based on a solar atlas (Chance and Kurucz, 2010) or on measured spectra of scattered sunlight. For weak absorbers, we can approximate the measured spectrum with the reference spectrum I_0. Scattering then adds an intensity $J = \sum_i J_i$ to the measured intensity $I = I_0 + J$. This will lead to an apparent absorption structure in the optical density τ_{Obs}. I is the measured intensity of the measurement spectrum, I_0 the intensity of the Fraunhofer reference spectrum.

$$\tau_{\mathrm{Obs}} = -\ln\left(\frac{I_0 + \sum_i J_i}{I_0}\right) \approx -\sum_i \frac{J_i}{I_0} \tag{19}$$

The additional measured intensities $J_i(\lambda)$ can be caused by RRS of N_2, O_2, VRS of N_2, O_2, water vapour or liquid water, but also by instrumental stray light leading to an (approximately) wavelength-independent intensity offset. Equation (19) is linear in J_i, therefore the different components can be fitted separately to the observed OD. $J_{\mathrm{VRS\_N_2}}(\lambda)$ can be calculated by shifting a sunlight spectrum in frequency by $\Delta\nu_{N_2}$ and scaling by $(\widetilde{\nu}_{\mathrm{in}} + \widetilde{\nu})^4$ and $J_{\mathrm{VRS\_O_2}}(\lambda)$ respectively (see Eq. 14). Under the assumption that the rotational Raman constant of N_2 and O_2 is independent of the vibrational state

AMTD
8, 3423–3469, 2015

(which is the case within 1.2 % for the $\nu = 0, 1$ states for O_2 and N_2, see Table 1), the intensity caused by vibrational-rotational transitions was calculated also using DOASIS.

The optical density τ_{VRS} can be fitted to correct for the additional intensity caused by vibrational Raman scattering, in this case based on solar atlas I^*, from which also J_{VRS} was calculated:

$$\tau_{VRS} = \frac{J_{VRS} \otimes H}{I^* \otimes H} \tag{20}$$

$I_0 = I^* \otimes H$ for the calculation of τ_{VRS} can also be calculated from a solar atlas I^* by convolution with the instrument function $H(\lambda, \lambda')$ of the instrument. This way, effects caused by the (typically unknown) quantum efficiency of the measuring spectrometer cancel out and do not introduce additional residual structures.

4 Results

The following two subsections describe two ways how to detect the VRS signature in measurement data: in the first approach the correction spectra are calculated and directly fitted to the measured optical densities. The obtained fit coefficients are compared to the Ring signal. In the second approach the residuals from a standard fit are analyzed systematically using a multi-linear regression. This offers the possibility to average over the residual spectra of a complete campaign to minimize photon shot noise. It furthermore yields estimates on the impact of VRS on the caclulated dSCDs of other absorbers.

4.1 Detection of the VRS signal in measurement data

The VRS correction spectra τ_{VRS} for N_2 and O_2 were calculated according to Eq. (20) from a solar atlas and then separately included in the spectral evaluation of the measurement data in the spectral range from 420–440 nm. This wavelength range has been chosen to avoid the main water vapour absorptions at 416 and 442 nm.

AMTD
8, 3423–3469, 2015

The results of the spectral analysis of 16 co-added elevation sequences (2 h time resolution) were filtered: only spectra with a low fit residual with a Root Mean Square (RMS) of less than 1.5×10^{-4} were used. This ensures that spectra during twilight and/or high NO_2 concentrations, which can increase the overall residual of the fit, are not included in the further analysis.

A comparison of the VRS and RRS signal is shown in Fig. 6. A clear correlation of the contribution of rotational Raman scattering with the contribution from vibrational Raman scattering on N_2 is observed ($R^2 = 0.8$). The contribution from O_2 is also positively correlated with the Raman signal, but the slope is nearly zero within the measurement error ($R^2 = 0.1$). The contributions from rotational-vibrational inelastic scattering was not identified in measurement spectra. In Table 6 the results are listed and compared to calculations.

The effective contribution to the measured intensity was estimated by using the Fraunhofer line at $\lambda = 430$ nm: The intensity caused by each of the processes, RRS, VRS N_2 and VRS O_2 at this wavelength will create a maximum in the respective pseudo cross-section $I_{\mathrm{Raman}_i}(\lambda)/I_0(\lambda)$, which then allows to estimate also constant intensity offsets due to these processes.

4.2 An alternative way of VRS signal detection

Alternatively, the optical density due to VRS can be extracted from residual spectra of a DOAS fit using only the cross-sections listed in Table 5. A schematic of both approaches is shown in Fig. 7. From the underlying properties of VRS described in Sect. 2 a linear relationship between the observed RRS and VRS signal is expected. This relationship is found for actual MAX-DOAS measurement data as shown in Fig. 6. Parameters which can modify this relation are discussed in Sect. 5.3.

In order to linearly decompose the residual spectra based on column densities obtained from the DOAS fit, a system of linear equations was set up to determine contributions $\boldsymbol{v}_i$ to the residual spectra $\mathbf{R}$ which are correlated with the column densities $\boldsymbol{S}_i$. The residual spectrum $\boldsymbol{v}_{\mathrm{Ring}}$ which is found to correlate with the Ring signal $\boldsymbol{S}_{\mathrm{Ring}}$

AMTD
8, 3423–3469, 2015

is then expected to contain the residual structures caused by VRS, independently of potential influences of other absorbers on the residual spectra. Insufficiently modeled absorption cross-sections of the absorber i are found in $\boldsymbol{v}_i$, if the respective dSCDs are not strongly correlated.

This approach is based on the following procedure:

1. The complete M91 MAX-DOAS data set was fitted from 420–440 nm to avoid the main water vapour absorptions at 416 and 442 nm. The retrieval was the same as in the first analysis (see Table 5), but without the VRS correction spectra and based on individual spectra with an exposure time of one minute.
2. Only fits with a RMS of $< 4 \times 10^{-4}$ were used for the multi-linear regression.
3. All channels j from the residual spectra i were stored in the matrix $\mathbf{R} = R_{ij}$.
4. Regressors were the dSCDs $\mathbf{S}$ calculated in 1., the size of the intensity offset correction, exposure time and number of scans to test if dark current/offset correction spectra might contribute to the residual. Together, these vectors form the matrix $\mathbf{A}$.

$$\mathbf{A}^{\mathrm{T}} \cdot \mathbf{V} = (\boldsymbol{S}_{\mathrm{Ring}} \quad \boldsymbol{S}_{\mathrm{H_2O}\cdots})^{\mathrm{T}} \cdot (\boldsymbol{v}_{\mathrm{Ring}} \quad \boldsymbol{v}_{\mathrm{H_2O}\cdots}) = \mathbf{R} \tag{21}$$

The overdetermined system of linear equations (Eq. 21) was solved for $\mathbf{V}$ using a least-squares approach, minimizing $|\mathbf{A}^{\mathrm{T}} \cdot \mathbf{V} - \mathbf{R}|_2$. This yields $\mathbf{V} = (\mathbf{A}\mathbf{A}^{\mathbf{T}})^{-1}\mathbf{A}\mathbf{R}$. The resulting correction $\boldsymbol{v}_{\mathrm{Ring}}$ corresponding to the Ring dSCD $\boldsymbol{S}_{\mathrm{Ring}}$ was then fitted with the already included absorbers from the original fit scenario and additionally the pseudo cross-section for vibrational and vibration-rotational Raman scattering of N_2 and O_2. This fit is shown in Fig. 8. Adding the other absorbers is necessary due to possible compensation of residual structures due to VRS by other absorbers within the first fits to obtain the residuals. In other vectors corresponding to other absorbers or parameters the structure associated with N_2/O_2-VRS was not found.

AMTD
8, 3423–3469, 2015

Despite the significantly better detection of the VRS signal of O_2 and N_2, the contribution of VRRS of both species could not be disentangled from the intensity offset correction.

The fit of the Ring-correlated residual structure shown in Fig. 8 yields more information than only the contribution of VRS to the observed OD: it also yields approximations for the changes of other involved trace gases in the respective spectral region, a factor with which the Ring signal can be multiplied to obtain the averaged effect on NO_2 e.g.: the fit yields a NO_2 fit coefficient of 7.65×10^{-12}. For a large Ring signal of 5×10^{25} molec cm^{-2} this results in a change of NO_2 dSCDs of $(3.8 \pm 0.4) \times 10^{14}$ molec cm^{-2}. This is larger than the estimate from individual fits shown in Fig. 9, because Fig. 9 combines all measurements with different Ring dSCDs.

The main advantage of this approach is that it allows to obtain an average over the residual structures associated with a certain absorber over the whole period of a campaign, e.g. a month or a year. This can reduce the influence of photon shot noise to a minimum. Furthermore an identification of the VRS signature from spectral data is possible for N_2 as well as for the weaker O_2 signal, which was not found to be significant in Fig. 6 for individual elevation sequences.

5 Discussion

The obtained results from measurements listed in Table 6 are in agreement with calculations. Since the average scattering angle is also between 0–180°, the relative size of the VRS contributions is found between both extrema of $d\sigma(\Theta)/d\Omega$ at 0 and 90°. While the impact of VRS of N_2 is clearly detected, the spectral signature of VRS of O_2 remains close to the instruments detection limit. It can clearly be detected by using analysing all residual spectra as described in Sect. 4.2.

AMTD
8, 3423–3469, 2015

5.1 Impact on trace gas retrievals

Ignoring the potentially significant impact of VRS can lead to systematic biases in the spectral evaluation. Since IO, NO_2, water vapour and glyoxal are trace gases typically absorbing in a spectral range which is mainly affected by VRS, its effect is exemplary studied for these trace-gases for our M91 data set. Also here 16 elevation sequences were co-added in order to reduce the overall fit errors. Fit results with an RMS larger than 2×10^{-4} were not used. We observed an agreement of the results when not co-adding elevation sequences.

We found that correcting for the effect of VRS will reduce the total RMS of the fit residual for a large Ring signal and thus in most cases also the fit error. It does not significantly lower the RMS for spectra with small Ring signals. Whether the correction has an impact on the retrieved column densities has to be tested for each trace gas and also for different spectral resolutions of the respective MAX-DOAS instruments, which can have an influence on the way in which the neglected apparent OD was compensated for. The difference of the squares of the RMS χ^2 of the evaluation with and without correcting for VRS is expected to have a linear relationship with the square of the Ring signal, R:

$$\Delta\chi^2 = a \cdot R^2 \tag{22}$$

This relation is found in MAX-DOAS data e.g. from M91, with $a = (0.25 \pm 0.05) \times 10^{-8}/(5 \times 10^{25}\,\mathrm{molec\,cm^{-2}})^2$ for the wavelength interval 420–438 nm, effectively reducing the RMS of a fit residual of 1×10^{-4} by about 15 % for a Ring signal of $5 \times 10^{25}\,\mathrm{molec\,cm^{-2}}$. In other words: if no VRS spectrum is included, the minimum possible RMS for a DOAS fit showing a Ring signal of this magnitude is larger than 5×10^{-5}. In this case, 30 % of the VRS signal is already compensated for by other absorbers and the intensity offset correction.

The following subsections show the impact on the spectral retrieval of different trace gases when neglecting this effect. It may vary depending on fit settings and the spectral resolution of the instrument.

AMTD
8, 3423–3469, 2015

5.1.1 Influence of VRS on the retrieval of IO

To estimate the influence of having ignored the effect of VRS of N_2, MAX-DOAS data from M91 was reanalysed for IO in the wavelength range from 418–438 nm with and without VRS and VRRS (N_2) correction spectra. Using an example measurement spectrum with 2×10^{-4} differential optical density caused by VRS from 432–438 nm, including the correction spectra led to a decrease of the fit error by 25 %. Leaving the size of the correction independent of the Ring spectrum showed that the IO dSCD is independent of the amount of structures caused by VRS of N_2 within the typical IO measurement error of 1.5×10^{12} molec cm^{-2}.

Using the linear regression method and the fit shown in Fig. 8 while assuming a maximum Ring signal of 5×10^{25} molec cm^{-2} this then corresponds to a change in IO dSCD of 6×10^{11} molec cm^{-2}, which is also within the typical IO measurement errors.

The effect of the VRRS ($\Delta\nu = 1, \Delta J \neq 0$) transitions was not observed to be correlated with RRS and could not be distinguished from the contribution by the intensity offset correction. Therefore, its impact on IO dSCDs was not studied.

5.1.2 Influence of VRS on the retrieval of NO_2

NO_2 can be evaluated in the same wavelength range as IO. In this wavelength range, NO_2 has a relatively large absorption cross-section of NO_2 and the influence of water vapour absorption is minimal. When retrieving tropospheric NO_2 dSCD, often negative NO_2 values are observed in clean and remote areas. Since these negative dSCD are also frequently observed close to local noon, this excludes an effect of a changing AMF of stratospheric NO_2 within one elevation sequence. Including the VRS correction spectra can lead to a reduction of the fit error by ≈ 15 % and furthermore the NO_2 dSCD changes by 4×10^{14} molec cm^{-2} per 2×10^{-4} VRS(N_2) contribution. This corresponds typically to a difference of 20 ppt NO_2 and can be thus significant for background measurements of NO_2 in clean areas. Figure 9 shows two histograms for NO_2 dSCDs from

AMTD
8, 3423–3469, 2015

M91, without (Reference fit) and with including a correction spectrum for VRS of N_2 and O_2.

Usually a wider fit interval (e.g. Richter et al., 2011) or a fit interval above 450 nm (e.g. Peters et al., 2012) is used to fit the absorptions of tropospheric NO_2, which will then reduce the relative effect from VRS(N_2), but the instrument needs to cover this wavelength range and the significantly stronger influence of water vapour absorption in this spectral range needs to be considered. The same analysis as shown in Fig. 9 for a fit range from 432–460 nm leads also leads to an underestimation of NO_2 dSCDs. A shift of the mean dSCD from 1.24×10^{14} molec cm^{-2} without including VRS(N_2) and VRS(O_2) correction spectra to a mean dSCD of 1.72×10^{14} molec cm^{-2} when including the correction is observed and is therefore within the typical fit error of 0.8×10^{14} molec cm^{-2}.

5.1.3 Influence of VRS on the retrieval of Glyoxal

To retrieve glyoxal, a fit window from 432–460 nm was used, with and without including N_2-VRS. Including a correction spectrum for N_2-VRS led to a reduction of fit RMS of 0–20 %, the glyoxal fit error was reduced by the same amount. RRS Ring spectrum and N_2 VRS also correlated in this wavelength window, despite the large water vapour absorption. The glyoxal dSCD increased when including the N_2-VRS for strong Ring spectrum signals of 5×10^{25} molec cm^{-2} by 6×10^{13} molec cm^{-2} and is thus clearly within the measurement error of typically 5×10^{14} molec cm^{-2}. All other influences, such as water vapour and O_4 absorption, have a far stronger influence on the spectral retrieval of glyoxal.

5.1.4 Influence of VRS on the retrieval of water vapour

The same settings as for glyoxal were used to estimate the influence of VRS on retrieved water vapour column densities. The observed changes were found to be below 1.5×10^{21} molec cm^{-2} (0.5 %) for typical dSCDs of $(3 \pm 1) \times 10^{23}$ molec cm^{-2} at telescope

AMTD
8, 3423–3469, 2015

elevation angles below 10°. This is the same magnitude as typical fit errors, which were reduced by 0–10 %.

For the narrower fit range from 420–440 nm, which is used e.g. for the evaluation shown in Fig. 8, the changes in apparent water vapour absorption are larger due to the smaller water vapour cross-section. Here the VRS would have changed the water vapour dSCD by up to 5×10^{22} molec cm^{-2} (typically more than 10 %) for a Ring signal of 5×10^{25} molec cm^{-2}.

The results from Lampel et al. (2015) reporting significant deviations of the relative absorption strengths for water vapour absorption in the blue wavelength range do not change significantly when applying correction spectra for N_2 and O_2 VRS in the spectral retrieval of the MAX-DOAS data.

5.2 Implications for other wavelength intervals

The influence of VRS on the observed differential OD at 433 and 436 nm is directly visible due to the high OD of the Ca-II-Fraunhofer lines, combined with overall small residual sizes due to large amounts of available light.

Towards shorter wavelengths, the amount of Raman scattered light scales with $1/\lambda^4$ according to Eq. (14). This is compensated, however, by the fact that Fraunhofer lines below 390 nm are less pronounced. In the wavelength range from 332–380 nm it was not possible to clearly identify the contribution of VRS of N_2/O_2. The residual spectra were dominated by systematic residual structures correlated with the dSCD of O_4 with typical ODs of $(4-8) \times 10^{-4}$ for light path lengths of ≈ 10 km. The structures were observed independently of the employed O_4 literature cross-section. We expect an apparent differential OD due to the contribution by VRS of N_2 to measured ODs of about 3×10^{-4} at 360 nm (see also Fig. 3) for a large Ring signal of 5×10^{25} molec cm^{-2}.

Strong absorbers such as e.g. ozone, water vapour or NO_2 need to be considered, if the incident light was attenuated by any strong absorber before scattered inelastically.

AMTD
8, 3423–3469, 2015

But even without strong Fraunhofer or absorption lines, this effect contributes to the observed differential OD according to Eq. (19). However, constant or polynomial intensity offset corrections are included in typical spectral evaluations of DOAS measurements, compensating for most of the contribution of VRS and VRRS.

5.3 Recommended corrections

Correction spectra for VRS need to be included especially in the spectral retrievals of NO_2, IO and glyoxal, but also water vapour in the blue spectral range, whenever wavelengths between 430–440 nm are included.

Since the atmospheric O_2/N_2 ratio is constant (at the precision relevant to correcting spectra for VRS contributions) , it is advisable as a first approximation to include only a single combined $N_2 + O_2$-spectrum compensating for VRS contributions to measured intensities. The contribution by VRRS is mostly proportional to the VRS signal and can therefore be added to the VRS correction spectrum. On the other hand, the contribution of VRRS is relatively smooth (compare Fig. 2) due to the rotational shifts of the transitions and a large part is already compensated in fit settings by the intensity offset correction. Given a Ring signal with an OD of e.g. 2 %, this translates to an additionally measured intensity due to VRRS of 0.8×10^{-4}. Due to the Raman remapped Ca lines the largest variations are expected for the spectral region between 414–440 nm. The effect is already corrected by the intensity offset correction except for a remaining part of 30–50 %, which translates to total differential ODs of $< 0.4 \times 10^{-4}$. This is currently negligible for most ground-based measurements, but this effect might need to be considered for geometries where a strong filling in of Fraunhofer lines is observed[1].

Due to the observed correlation of the spectral signature of VRS scattering on N_2 and the Ring dSCD shown in Fig. 5, a direct correction of the Ring spectrum together with the VRS signal seems reasonable, at least in the spectral ranges where an effect has been observed. The actual values of the cross-sections can be found e.g. in Table 6.

[1] All calculations for a spectral resolution of the instrument of 0.5 nm.

AMTD
8, 3423–3469, 2015

This would allow furthermore to correct for VRRS scattering, which is also expected to behave in the same way as the Ring spectrum, but is often (by coincidence) corrected by the intensity offset correction (see Eq. 19), as estimated above. This correction of the Ring spectrum would therefore improve how the intensity offset correction can be interpreted, which usually has been introduced in the first place to compensate for instrumental stray light. The contribution of the VRRS on O_2 and N_2 can then be removed from the additive polynomial, because the dominating factor for determining the Ring spectrum dSCD is the actual RRS contribution, which is about fifty times larger.

However, the following points need to be considered:

1. Vibrational Raman scattering leads to a red-shift of solar radiation, thus the ratio of vibrational Raman scattered and elastically scattered light is influenced by the wavelength dependency of the aerosol extinction and Rayleigh scattering. For the case of rotational Raman scattering (the Ring effect) this is inherently compensated for, since the frequency shift due to RRS is not significant for the wavelength dependence of the aerosol extinction. For the shift of 40 nm of N_2 VRS from the Ca-II K Fraunhofer line at 393 nm, significant relative intensity differences at 393/433 nm can be observed for different measurement geometries and/or aerosol loads. During M91 relative intensities at 390 and 432 nm, the so called colour-index CI(390, 432 nm), were observed between 0.3 and 0.8 for zenith sky measurements, even more if considering the complete elevation angle sequence. This relation translates directly to the size of VRS correction spectrum via Eq. (19). Therefore, a direct correction of the Ring spectrum is not possible in general, if not considering these effects explicitly. The same argumentation can be applied for separating the influence of VRS(N_2) and VRS(O_2), since the wavelength shifts are different. However, the influence of VRS(O_2) is hardly detected in current measurement spectra. A potential dependence of VRS(N_2)-OD on the colour-index was not observed in measurement data.

AMTD
8, 3423–3469, 2015

2. The phase functions of RRS, VRS and VRRS differ. Different contributions proportional to $\overline{\alpha_{ij}^2}$ and $\overline{\alpha_{ii}^2}$ in the cross-section correspond to different phase functions, thus the resulting filling-in does not need to be correlated exactly. This needs to be modelled in detail to estimate the error made when assuming the same phase functions. Since no explicit dependence of the relative VRS contribution to the Ring signal depending on the measurement geometry was observed during one month of measurements shown in Table 6, it is estimated to be below 20 % of the OD of the VRS of N_2. For a typical variation of the Ring dSCD of 3×10^{25} molec cm^{-2} this error is therefore found to be below 2×10^{-5} peak-to-peak in the wavelength range between 430–440 nm, where the largest spectral structures were detected. This is five times smaller than the typical sizes of residual spectra of current MAX-DOAS evaluations.

A way to avoid these points is to use a measured spectrum, which includes the effects due to changes in radiative transfer, such as aerosol and measurement geometry. When using measured spectra, this would require the same quantum efficiency of the instrument at both wavelengths or a radiometrically calibrated instrument, as well as a constant instrument function.

It is therefore recommended to include the correction spectrum for VRS of N_2 without including the contribution from VRRS, calculated based on a solar atlas. Correction for VRS of O_2 is only needed if the RMS of the residual is significantly below 10^{-4}.

6 Conclusions

Vibrational Raman scattering can contribute significantly to observed optical densities in passive DOAS applications, such as satellite-, airborne and ground-based MAX-DOAS measurements. Optical densities due to VRS Fraunhofer "ghosts" were observed to amount to up to 2.5×10^{-4} in the blue spectral region. In spectral regions

AMTD
8, 3423–3469, 2015

without large Fraunhofer ghost structures the offset polynomial typically used in DOAS evaluations can compensate for most of this effect.

The apparent OD caused by VRS can influence the spectral retrieval of various trace gases. For instance, the large Ca-II-Fraunhofer lines at 393.4 and 396.8 nm lead to ghost lines at 433.1 and 437.2 nm. The additional measured intensity can influence the spectral retrieval of NO_2, water vapour, IO and Glyoxal. This influence was studied for ship-based MAX-DOAS measurements. While the influence on the total magnitude of water vapour, IO and glyoxal column densities was below the detection limit, a significant and systematic negative offset of NO_2 dSCDs by up to 4×10^{14} molec cm^{-2} was observed. In all cases the fit errors were reduced by up to 20 % by including the VRS spectrum in the DOAS fit.

The systematic biases introduced into DOAS evaluations of different trace gases by neglecting the effect of vibrational Raman scattering shows once more the need for high-precision absorption measurements of trace gases and thorough statistical analysis of residual spectra. Even if individual measurements hardly allow the identification of systematic structures, systematic contribution in the residual spectra might still be identified and point towards possible improvements. Future advances in DOAS evaluations as well as improved DOAS instruments are expected to further reduce the magnitude of residual structures and thus improve detection limits. While the correction of VRS effects already improves the evaluation of several trace species, this correction will be even more important in future, advanced DOAS evaluations.

Acknowledgements. We thank H. Haug for laying the foundations for this work in his diploma thesis (Haug, 1996). We thank Stefan Schmitt for valuable comments during the preparation of this manuscript.

We thank the captain, officers and crew for support during research cruise M91.

We thank the German Science foundation DFG for its support within the core program METEOR/MERIAN.

We thank the German ministry of education and research (BMBF) for supporting this work within the SOPRAN (Surface Ocean Processes in the Anthropocene) project (Förderkennzahl: 03F0662F) which is embedded in SOLAS.

AMTD
8, 3423–3469, 2015

We thank the authorities of Peru for the permission to work in their territorial waters.
We thank GEOMAR for logistic support.
Rich Pawlowicz is acknowledged for providing the m_map toolbox.

The article processing charges for this open-access publication
have been covered by the Max Planck Society.

References

Aliwell, S. R., Roozendael, M. V., Johnston, P. V., Richter, A., Wagner, T., Arlander, D. W., Burrows, J. P., Jones, D. J., Tornkvist, K. K., Lambert, J.-C., Pfeilsticker, K., and Pundt, I.: Analysis for BrO in zenith-sky spectra: an intercomparision exercise for analysis improvement, J. Geophys. Res., 107, D14, doi:10.1029/2001JD000329, 2002. 3425

Bange, H.: Surface ocean – lower atmosphere study (SOLAS) in the upwelling region off Peru – cruise no. M91, DFG-Senatskommission fuer Ozeanographie, METEOR-Berichte, Bremen, Germany, 91, 69 pp., doi:10.2312/cr_m91, 2013. 3433

Bates, D.: Rayleigh scattering by air, Planet. Space Sci., 32, 785–790, 1984. 3430

Burrows, J., Platt, U., Chance, K., Vountas, M., Rozanov, V., Richter, A., Haug, H., and Marquard, L.: Study of the Ring Effect, European Space Agency, Noordivijk, the Netherlands, 1996. 3425

Bussemer, M.: Der Ring-Effekt: Ursachen und Einfluß auf die spektroskopische Messung stratosphärischer Spurenstoffe, Diploma thesis, Heidelberg University, Heidelberg, Germany, 1993. 3434, 3459

Chance, K. and Kurucz, R.: An improved high-resolution solar reference spectrum for earth's atmosphere measurements in the ultraviolet, visible, and near infrared, J. Quant. Spectrosc. Ra., 111, 1289–1295, 2010. 3434, 3436

Coburn, S., Dix, B., Sinreich, R., and Volkamer, R.: The CU ground MAX-DOAS instrument: characterization of RMS noise limitations and first measurements near Pensacola, FL of BrO, IO, and CHOCHO, Atmos. Meas. Tech., 4, 2421–2439, doi:10.5194/amt-4-2421-2011, 2011. 3426

AMTD
8, 3423–3469, 2015

Dinter, T., Rozanov, V. V., Burrows, J. P., and Bracher, A.: Retrieving the availability of light in the ocean utilising spectral signatures of Vibrational Raman Scattering in hyper-spectral satellite measurements, Ocean Sci. Discuss., 12, 31–81, doi:10.5194/osd-12-31-2015, 2015. 3427
Fish, D. and Jones, R.: Rotational Raman scattering and the ring effect in zenith-sky spectra, Geophys. Res. Lett., 22, 811–814, 1995. 3425
Frieß, U., Sihler, H., Sander, R., Pöhler, D., Yilmaz, S., and Platt, U.: The vertical distribution of BrO and aerosols in the Arctic: measurements by active and passive differential optical absorption spectroscopy, J. Geophys. Res.-Atmos., 116, D14, doi:10.1029/2011JD015938, 2011. 3425
Grainger, J. and Ring, J.: Anomalous fraunhofer line profiles, Nature, 193, 762, 1962. 3425
Greenblatt, G. D., Orlando, J. J., Burkholder, J. B., and Ravishankara, A. R.: Absorption measurements of oxygen between 330 and 1140 nm, J. Geophys. Res., 95, 18577–18582, 1990. 3436
Großmann, K., Frieß, U., Peters, E., Wittrock, F., Lampel, J., Yilmaz, S., Tschritter, J., Sommariva, R., von Glasow, R., Quack, B., Krüger, K., Pfeilsticker, K., and Platt, U.: Iodine monoxide in the Western Pacific marine boundary layer, Atmos. Chem. Phys., 13, 3363–3378, doi:10.5194/acp-13-3363-2013, 2013. 3425, 3433, 3435
Haltrin, V. I. and Kattawar, G. W.: Self-consistent solutions to the equation of transfer with elastic and inelastic scattering in oceanic optics: I. model, Appl. Optics, 32, 5356–5367, 1993. 3427
Haug, H.: Raman-Streuung von Sonnenlicht in der Erdatmosphäre, Diploma thesis, Institut für Umweltphysik, Ruprecht-Karls-Universität Heidelberg, Heidelberg, 1996. 3427, 3448
Hendrick, F., Pommereau, J.-P., Goutail, F., Evans, R. D., Ionov, D., Pazmino, A., Kyrö, E., Held, G., Eriksen, P., Dorokhov, V., Gil, M., and Van Roozendael, M.: NDACC/SAOZ UV-visible total ozone measurements: improved retrieval and comparison with correlative ground-based and satellite observations, Atmos. Chem. Phys., 11, 5975–5995, doi:10.5194/acp-11-5975-2011, 2011. 3425
Hermans, C., Vandaele, A. C., Carleer, M., Fally, S., Colin, R., Jenouvrier, A., Coquart, B., and Mérienne, M.-F.: Absorption cross-sections of atmospheric constituents: NO_2, O_2, and H_2O, Environ. Sci. Pollut. R., 6, 151–158, 1999. 3436
Hönninger, G. and Platt, U.: Observations of BrO and its vertical distribution during surface ozone depletion at alert, Atmos. Environ., 36, 2481–2489, 2002. 3432
Irikura, K. K.: Experimental vibrational zero-point energies: diatomic molecules, J. Phys. Chem. Ref. Data, 36, 389–397, 2007. 3455

AMTD
8, 3423–3469, 2015

Joiner, J. and Bhartia, P.: The determination of cloud pressures from rotational raman scattering in satellite backscatter ultraviolet measurements, J. Geophys. Res.-Atmos., 100, 23019–23026, 1995. 3425

Joiner, J., Bhartia, P. K., Cebula, R. P., Hilsenrath, E., McPeters, R. D., and Park, H.: Rotational raman scattering (ring effect) in satellite backscatter ultraviolet measurements, Appl. Optics, 34, 4513–4525, 1995. 3425

Kraus, S.: DOASIS – A Framework Design for DOAS, Dissertation, Heidelberg University, Heidelberg, 2006. 3434, 3459

Lampel, J., Pöhler, D., Tschritter, J., Frieß, U., and Platt, U.: On the relative absorption strengths of water vapor in the blue wavelength range, Atmos. Meas. Tech. Discuss. in preparation, 2015. 3435, 3444, 3459

Long, D. A.: The Raman Effect: A Unified Treatment of the Theory of Raman Scattering by Molecules, John Wiley & Sons Ltd, Chichester, England, 2002. 3428, 3430, 3458

Mahajan, A. S., Prados-Roman, C., Hay, T. D., Lampel, J., Pöhler, D., Großmann, K., Tschritter, J., Frieß, U., Platt, U., Johnston, P., Kreher, K., Wittrock, F., Burrows, J. P., Plane, J. M., and Saiz-Lopez, A.: Glyoxal observations in the global marine boundary layer, J. Geophys. Res.-Atmos., 119, 10, doi:10.1002/2013JD021388, 2014. 3425, 3435

Murphy, W. F.: The rovibrational Raman spectrum of water vapour v1 and v3, Mol. Phys., 36, 727–732, 1978. 3426

Penney, C. M., Peters, R. L. S., and Lapp, M.: Absolute rotational raman cross sections for N_2, O_2, and CO_2, J. Opt. Soc. Am., 64, 712–716, 1974. 3426, 3430

Peters, E., Wittrock, F., Großmann, K., Frieß, U., Richter, A., and Burrows, J. P.: Formaldehyde and nitrogen dioxide over the remote western Pacific Ocean: SCIAMACHY and GOME-2 validation using ship-based MAX-DOAS observations, Atmos. Chem. Phys., 12, 11179–11197, doi:10.5194/acp-12-11179-2012, 2012. 3425, 3443

Peters, E., Wittrock, F., Richter, A., Alvarado, L. M. A., Rozanov, V. V., and Burrows, J. P.: Liquid water absorption and scattering effects in DOAS retrievals over oceans, Atmos. Meas. Tech., 7, 4203–4221, doi:10.5194/amt-7-4203-2014, 2014. 3435

Pinardi, G., Van Roozendael, M., Abuhassan, N., Adams, C., Cede, A., Clémer, K., Fayt, C., Frieß, U., Gil, M., Herman, J., Hermans, C., Hendrick, F., Irie, H., Merlaud, A., Navarro Comas, M., Peters, E., Piters, A. J. M., Puentedura, O., Richter, A., Schönhardt, A., Shaiganfar, R., Spinei, E., Strong, K., Takashima, H., Vrekoussis, M., Wagner, T., Wittrock, F., and Yilmaz, S.: MAX-DOAS formaldehyde slant column measurements during CINDI: intercomparison

AMTD
8, 3423–3469, 2015

and analysis improvement, Atmos. Meas. Tech., 6, 167–185, doi:10.5194/amt-6-167-2013, 2013. 3425

Platt, U. and Stutz, J.: Differential Optical Absorption Spectroscopy, Springer, Berlin, Heidelberg, 2008. 3425, 3427, 3432

Platt, U., Marquard, L., Wagner, T., and Perner, D.: Corrections for zenith scattered light DOAS, Geophys. Res. Lett., 24, 1759–1762, 1997. 3427

Richter, A., Begoin, M., Hilboll, A., and Burrows, J. P.: An improved NO_2 retrieval for the GOME-2 satellite instrument, Atmos. Meas. Tech., 4, 1147–1159, doi:10.5194/amt-4-1147-2011, 2011. 3435, 3443

Rizi, V., Iarlori, M., Rocci, G., and Visconti, G.: Raman LIDAR observations of cloud liquid water, Appl. Optics, 43, 6440–6453, 2004. 3426

Roscoe, H. K., Van Roozendael, M., Fayt, C., du Piesanie, A., Abuhassan, N., Adams, C., Akrami, M., Cede, A., Chong, J., Clémer, K., Friess, U., Gil Ojeda, M., Goutail, F., Graves, R., Griesfeller, A., Grossmann, K., Hemerijckx, G., Hendrick, F., Herman, J., Hermans, C., Irie, H., Johnston, P. V., Kanaya, Y., Kreher, K., Leigh, R., Merlaud, A., Mount, G. H., Navarro, M., Oetjen, H., Pazmino, A., Perez-Camacho, M., Peters, E., Pinardi, G., Puentedura, O., Richter, A., Schönhardt, A., Shaiganfar, R., Spinei, E., Strong, K., Takashima, H., Vlemmix, T., Vrekoussis, M., Wagner, T., Wittrock, F., Yela, M., Yilmaz, S., Boersma, F., Hains, J., Kroon, M., Piters, A., and Kim, Y. J.: Intercomparison of slant column measurements of NO_2 and O_4 by MAX-DOAS and zenith-sky UV and visible spectrometers, Atmos. Meas. Tech., 3, 1629–1646, doi:10.5194/amt-3-1629-2010, 2010. 3425

Rothman, L., Gordon, I., Babikov, Y., Barbe, A., Benner, D. C., Bernath, P., Birk, M., Bizzocchi, L., Boudon, V., Brown, L., Campargue, A., Chance, K., Cohen, E., Coudert, L., Devi, V., Drouin, B., Fayt, A., Flaud, J.-M., Gamache, R., Harrison, J., Hartmann, J.-M., Hill, C., Hodges, J., Jacquemart, D., Jolly, A., Lamouroux, J., Roy, R. L., Li, G., Long, D., Lyulin, O., Mackie, C., Massie, S., Mikhailenko, S., Müller, H., Naumenko, O., Nikitin, A., Orphal, J., Perevalov, V., Perrin, A., Polovtseva, E., Richard, C., Smith, M., Starikova, E., Sung, K., Tashkun, S., Tennyson, J., Toon, G., Tyuterev, V., and Wagner, G.: The HITRAN2012 molecular spectroscopic database, J. Quant. Spectrosc. Ra., 130, 4–50, 2013. 3435, 3459

Schönhardt, A., Richter, A., Wittrock, F., Kirk, H., Oetjen, H., Roscoe, H. K., and Burrows, J. P.: Observations of iodine monoxide columns from satellite, Atmos. Chem. Phys., 8, 637–653, doi:10.5194/acp-8-637-2008, 2008. 3425

AMTD
8, 3423–3469, 2015

Schrötter, H. and Klöckner, H.: Raman scattering cross sections in gases and liquids, in: Raman Spectroscopy of Gases and Liquids, edited by: Weber, A., Volume 11 of Topics in Current Physics, pages 123–166, Springer, Berlin, Heidelberg, 1979. 3431

Serdyuchenko, A., Gorshelev, V., Weber, M., Chehade, W., and Burrows, J. P.: High spectral resolution ozone absorption cross-sections – Part 2: Temperature dependence, Atmos. Meas. Tech., 7, 625–636, doi:10.5194/amt-7-625-2014, 2014. 3435, 3459

Sinreich, R., Coburn, S., Dix, B., and Volkamer, R.: Ship-based detection of glyoxal over the remote tropical Pacific Ocean, Atmos. Chem. Phys., 10, 11359–11371, doi:10.5194/acp-10-11359-2010, 2010. 3435

Solomon, S., Schmeltekopf, A. L., and Sanders, R. W.: On the interpretation of zenith sky absorption measurements, J. Geophys. Res.-Atmos., 92, 8311–8319, 1987. 3425

Spietz, P., Gómez Martín, J. C., and Burrows, J. P.: Spectroscopic studies of the I_2/O_3 photochemistry: Part 2. improved spectra of iodine oxides and analysis of the IO absorption spectrum, J. Photoch. Photobio. A, 176, 50–67, 2005. 3459

Thalman, R. and Volkamer, R.: Temperature dependent absorption cross-sections of O_2–O_2 collision pairs between 340 and 630 nm and at atmospherically relevant pressure, Phys. Chem. Chem. Phys., 15, 15371–15381, 2013. 3436, 3459

Vandaele, A., Hermans, C., Simon, P., Carleer, M., Colin, R., Fally, S., Merienne, M., Jenouvrier, A., and Coquart, B.: Measurements of the NO_2 absorption cross-section from 42 000 to 10 000 cm^{-1} (238–1000 nm) at 220 K and 294 K, J. Quant. Spectrosc. Ra., 59, 171–184, 1998. 3459

Vandaele, A. C., Fayt, C., Hendrick, F., Hermans, C., Humbled, F., Van Roozendael, M., Gil, M., Navarro, M., Puentedura, O., Yela, M., Braathen, G., Stebel, K., Tørnkvist, K., Johnston, P., Kreher, K., Goutail, F., Mieville, A., Pommereau, J.-P., Khaikine, S., Richter, A., Oetjen, H., Wittrock, F., Bugarski, S., Frieß, U., Pfeilsticker, K., Sinreich, R., Wagner, T., Corlett, G., and Leigh, R.: An intercomparison campaign of ground-based uv-visible measurements of NO_2, BrO, and OClO slant columns: Methods of analysis and results for NO_2, J. Geophys. Res.-Atmos., 110, D8, doi:10.1029/2004JD005423, 2005. 3425

Volkamer, R., Spietz, P., Burrows, J. P., and Platt, U.: High-resolution absorption cross-section of glyoxal in the UV/vis and IR spectral ranges, J. Photoch. Photobio. A, 172, 35–46, 2005. 3459

AMTD
8, 3423–3469, 2015

Vountas, M., Rozanov, V. V., and Burrows, J. P.: Impact of rotational Raman scattering on radiative transfer in earth's atmosphere, J. Quant. Spectrosc. Ra., 60, 943–961, 1998. 3425, 3427

Vountas, M., Richter, A., Wittrock, F., and Burrows, J. P.: Inelastic scattering in ocean water and its impact on trace gas retrievals from satellite data, Atmos. Chem. Phys., 3, 1365–1375, doi:10.5194/acp-3-1365-2003, 2003. 3427, 3435

Wagner, T., Deutschmann, T., and Platt, U.: Determination of aerosol properties from MAX-DOAS observations of the Ring effect, Atmos. Meas. Tech., 2, 495–512, doi:10.5194/amt-2-495-2009, 2009. 3435, 3459

Wagner, T., Andreae, M. O., Beirle, S., Dörner, S., Mies, K., and Shaiganfar, R.: MAX-DOAS observations of the total atmospheric water vapour column and comparison with independent observations, Atmos. Meas. Tech., 6, 131–149, doi:10.5194/amt-6-131-2013, 2013. 3425

Weitkamp, C.: Range-resolved optical remote sensing of the Atmosphere, Springer, NY, USA, 2005. 3426, 3457

AMTD
8, 3423–3469, 2015

Table 1. The rotational constant B_0 and the vibrational constant $\widetilde{\nu}$ for ground state N_2 and O_2 according to Irikura (2007). For excited vibrational states $v > 0$ the rotational constant is modified: $B_v = B_0 - v \cdot \alpha_e$. These constants are used in Eq. (5) to calculate the energy of the molecule $E(v, J)$.

Molecule	B_0 [cm^{-1}]	$\widetilde{\nu}$ [cm^{-1}]	α_e [cm^{-1}]
N_2	1.98958	2329.9	0.01732
O_2	1.43765	1556.3	0.01593

AMTD
8, 3423–3469, 2015

Table 2. The statistical weight factor g_J due to nuclear spin (I) statistics for odd and even shell angular momentum J of the respective N_2 or O_2 molecule.

Molecule	I	g_J	g_J
J		odd	even
N_2	1	3	6
O_2	0	0	1

AMTD
8, 3423–3469, 2015

Table 3. Averaged polarisability a, a' and anisotropy γ, γ' according to Weitkamp (2005) and references therein for incident wavelengths between 400–500 nm. The resulting differential cross-sections $d\sigma/d\Omega$ are listed in Table 6.

Molecule	a^2 $m^6/(4\pi\epsilon_0)^2$	γ^2 $m^6/(4\pi\epsilon_0)^2$	a'^2 $m^4\,kg^{-1}/(4\pi\epsilon_0)^2$	γ'^2 $m^4\,kg^{-1}/(4\pi\epsilon_0)^2$
N_2	3.17×10^{-60}	0.52×10^{-60}	2.62×10^{-14}	4.23×10^{-14}
O_2	2.66×10^{-60}	1.26×10^{-60}	1.63×10^{-14}	6.46×10^{-14}

AMTD
8, 3423–3469, 2015

Table 4. Spatial averaged polarisation tensor according to Long (2002) and corresponding phase functions $f(\Theta)$.

	Transition	$\overline{[\alpha^2_{ii}]_{(v,J\to v',J')}}$	$\overline{[\alpha^2_{ij}]_{(v,J\to v',J')}}$
Cabannes	$\Delta v = 0, \Delta J = 0$	$a^2 + \frac{4}{45} b_{J\to J} \gamma^2$	$\frac{1}{15} b_{J\to J} \gamma^2$
RRS	$\Delta v = 0, \Delta J = \pm 2$	$\frac{4}{45} b_{J\to J\pm 2} \gamma^2$	$\frac{1}{15} b_{J\to J\pm 2} \gamma^2$
VRS	$\Delta v = 1, \Delta J = 0$	$\left(a'^2 + \frac{4}{45} b_{J\to J} \gamma'^2\right) \frac{h}{8c\pi^2\tilde{\nu}}$	$\left(\frac{1}{15} b_{J\to J} \gamma'^2\right) \frac{h}{8c\pi^2\tilde{\nu}}$
VRRS	$\Delta v = 1, \Delta J = \pm 2$	$\left(\frac{4}{45} b_{J\to J\pm 2} \gamma'^2\right) \frac{h}{8c\pi^2\tilde{\nu}}$	$\left(\frac{1}{15} b_{J\to J\pm 2} \gamma'^2\right) \frac{h}{8c\pi^2\tilde{\nu}}$
$f(\Theta)$		$1 + \cos^2(\Theta)$	$3 - \cos^2(\Theta)$

AMTD
8, 3423–3469, 2015

Table 5. Cross-sections used for the spectral (DOAS) retrieval. All shift and squeeze parameters of the cross-sections were linked, those of Ring and reference spectrum were linked separately.

Absorber	Source	dSCD for I_0 correction
NO_2 294 K	Vandaele et al. (1998)	1×10^{15} molec cm^{-2}
O_3 223 K	Serdyuchenko et al. (2014)	1×10^{18} molec cm^{-2}
IO	Spietz et al. (2005)	1×10^{13} molec cm^{-2}
H2O	Rothman et al. (2013) with corrections Lampel et al. (2015)	3×10^{23} molec cm^{-2}
Glyoxal	Volkamer et al. (2005) (Glyoxal only)	5×10^{14} molec cm^{-2}
O_4 293 K	Thalman and Volkamer (2013) (Glyoxal only)	3×10^{43} molec^{-2} cm^{-5}
Polynomial	third order	
Ring	by DOASIS (Kraus, 2006) and Bussemer (1993)	
Ring $\cdot\lambda^4$	Wagner et al. (2009)	
Intensity offset correction	zeroth order	

AMTD
8, 3423–3469, 2015

Table 6. Cross-sections for different contributions to Raman scattered light. Absolute values are listed as well as relative contributions, compared to RRS. The cross-sections were scaled according to the atmospheric ratio of 80 and 20 % for N_2 and O_2. These values are compared to the results from MAX-DOAS measurements during M91, directly from Fig. 6 and derived from the solution of a system of linear equations and resulting in a fit, which is shown in Fig. 8. The spectrum obtained from the linear system of equations had an 1σ-error of about 10 %. The VRRS contributions were not significant in either case. The theoretical cross-sections were calculated using Eq. (6) at 433 nm for RRS and at 393 nm for VRS.

		Calculation $d\sigma/d\Omega$				Measurements	
		$\Theta = 0^\circ$		$\Theta = 90^\circ$		Spectral Retrieval Fig. 6	Linear Regr. Fig. 8
		$cm^2\ sr^{-1}\ molec^{-1}$	%	$cm^2\ sr^{-1}\ molec^{-1}$	%	%	%
(1)	RRS (N_2/O_2)	3.4×10^{-29}	100	3.2×10^{-29}	100	100	100
(2)	N_2 VRS	1.2×10^{-30}	3.47	6.2×10^{-31}	1.96	2.5 ± 0.5	2.1 ± 0.3
(3)	N_2 VRRS	2.1×10^{-31}	0.60	1.9×10^{-31}	0.60		
(4)	O_2 VRS	3.4×10^{-31}	1.00	1.9×10^{-31}	0.60	0.4 ± 0.5	0.56 ± 0.2
(5)	O_2 VRRS	1.4×10^{-31}	0.40	1.25×10^{-31}	0.39		

AMTD
8, 3423–3469, 2015

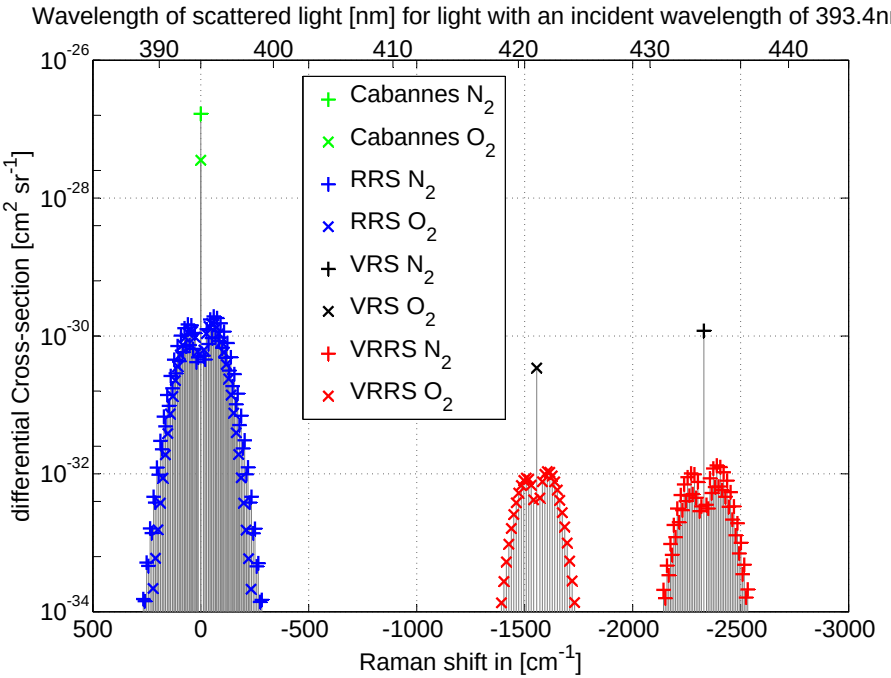

Figure 1. Cross-section of Cabannes line, rotational (RRS), vibrational (VRS) and rotational-vibrational Raman scattering (VRRS) for a wavelength of 393 nm scaled with 0.8 for N_2 and 0.2 for O_2 to reflect their atmospheric concentrations (see also Table 6). The cross-sections were calculated according to Eq. (1) at a scattering angle of $\Theta = 180^{\circ}$.

AMTD
8, 3423–3469, 2015

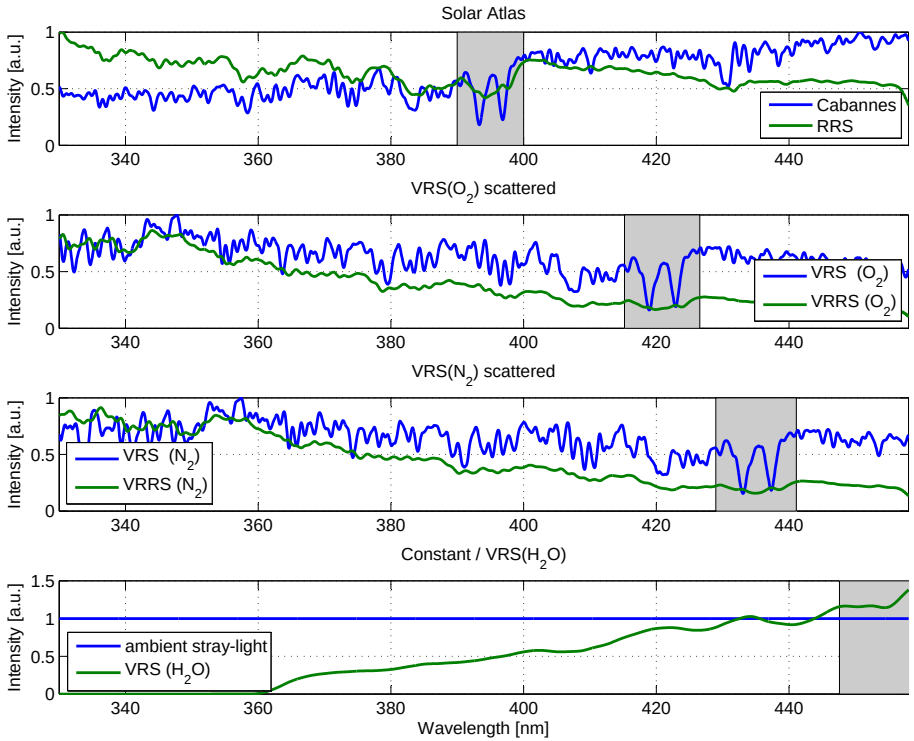

Figure 2. Calculated intensities (in arbitrary units) for purely Rayleigh scattered light (Cabannes), rotational Raman scattered light (RRS), vibrational Raman scattered light (VRS), and combined scattering (VRRS) due to N_2, O_2 and liquid water as well as assumed instrumental stray-light as a function of wavelength at a spectral resolution of 0.5 nm. The apparent optical densities I_{add}/I_0 according to Eq. (19) are shown in Fig. 3. The relative magnitudes for each of the effects are arbitrarily scaled. Note the red-shift in the VRS(O_2) and VRS(N_2) spectrum compared to the solar atlas; the Ca-II lines and their respective ghost lines for inelastic scattering on N_2, O_2 and liquid water are marked gray. For absolute magnitudes compare Table 6.

AMTD
8, 3423–3469, 2015

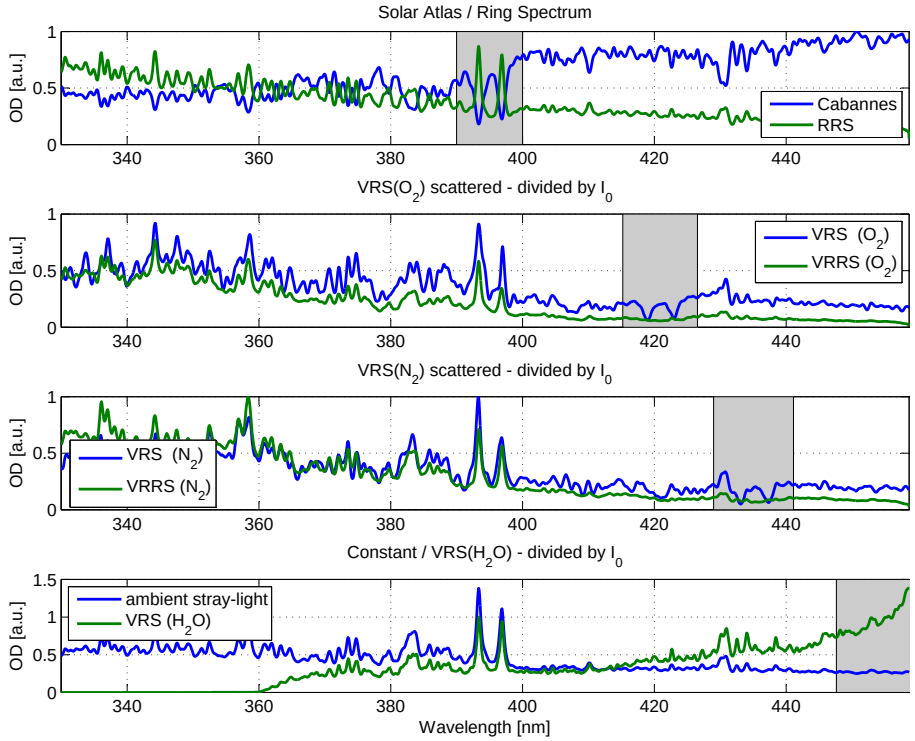

Figure 3. The apparent optical densities according to Eq. (19) related to the additional intensities in Fig. 2.

AMTD
8, 3423–3469, 2015

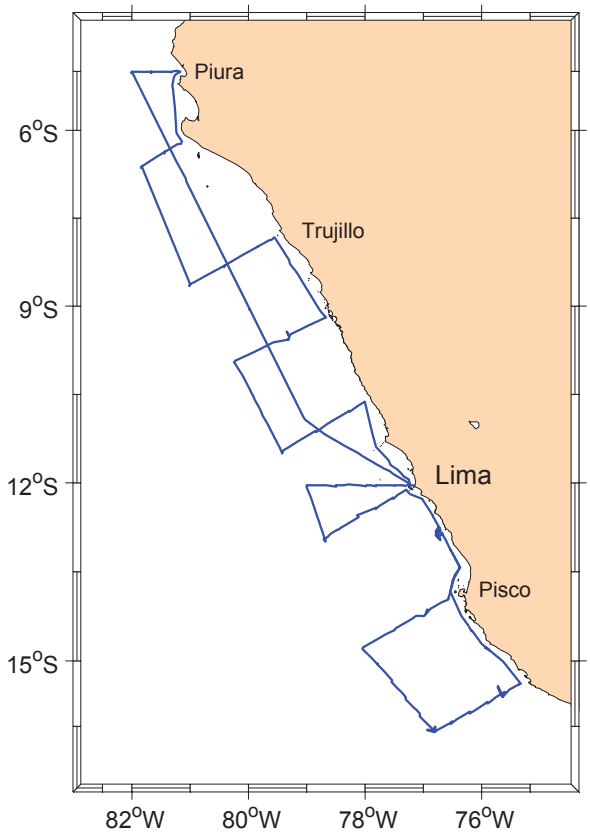

Figure 4. Track of cruise *Meteor M91*. From Lima, the ship first sailed north until about Piura and then continued south along transects from the open ocean to the coastal upwelling or vice versa until 18° S, from where it returned to Lima.

AMTD
8, 3423–3469, 2015

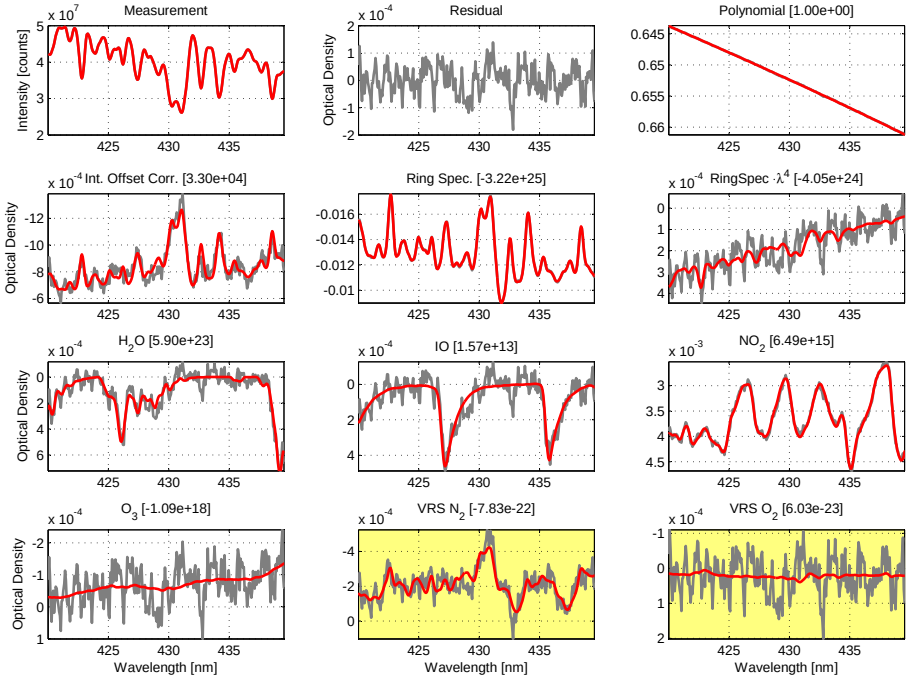

Figure 5. Fit showing the detection of structures from vibrational Raman scattering on N_2. The main peak at 430 nm originates from the reciprocal of a Fraunhofer structure at this wavelength from the Taylor expansion of the optical thickness. It vanishes when orthogonalizing the spectrum with the stray light compensation spectrum $1/I_0$. The two minima to at 432 and 436 nm are the red-shifted Calcium Fraunhofer lines. The grey lines are measured quantities, the red line is the modelled OD. The spectrum was recorded on 15 December 2012, starting at 17:38 UTC, at 12°33′ S, 76°50′ W at an SZA of 14° and a relative SAA of 132°. The FRS spectrum was recorded at 40° elevation. 16 elevation sequences were co-added. The Fraunhofer reference spectrum was omitted for clarity. Column densities are given in molec cm^{-2}.

AMTD
8, 3423–3469, 2015

Impact of vibrational raman scattering on DOAS measurements of atmospheric trace gases

J. Lampel et al.

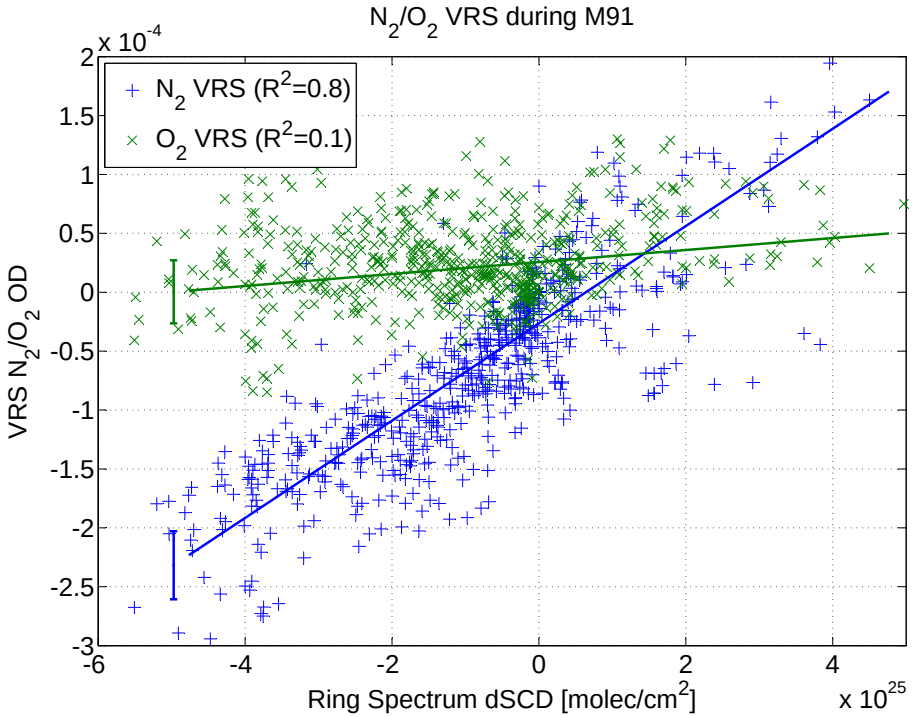

Figure 6. Fit coefficients for Ring and vibrational Raman correction spectrum for N_2 and O_2 from 702 co-added elevation sequences. The VRS axis shows the optical density of the of the Raman-remapped Ca lines. The resulting relative size of the RRS and VRS cross-sections are listed in Table 6. The intercept of the linear fits is in both cases within the typical measurement error shown as errorbars on the left.

AMTD
8, 3423–3469, 2015

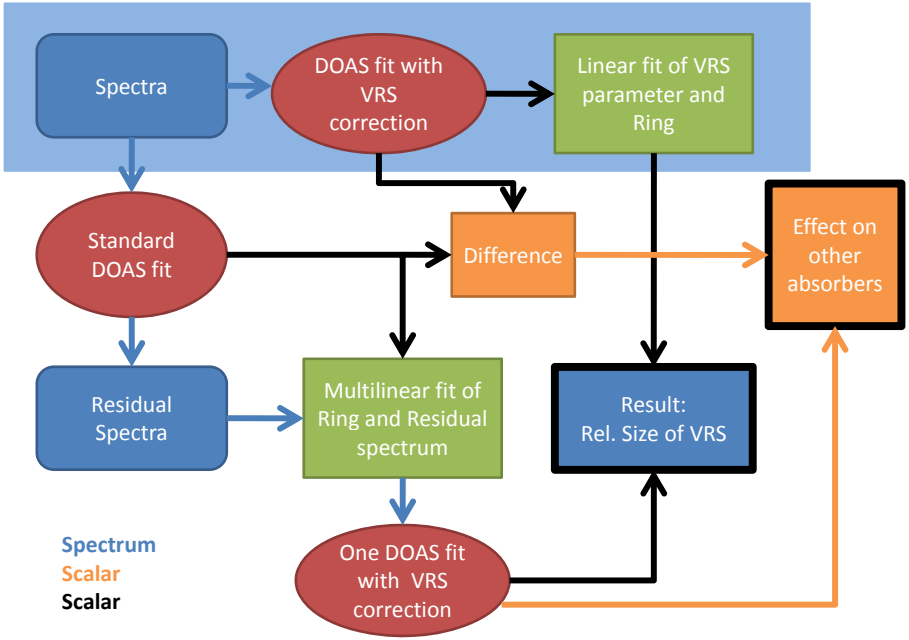

Figure 7. The first line of this diagram shows the procedure which led to Fig. 5: The VRS correction spectrum is added to the fit scenario, applied to all spectra and then the obtained fit coefficients are correlated with the Ring signal. The other approach (Sect. 4.2) uses a standard DOAS fit (without VRS correction), correlates the residuals with the obtained coefficients from the fit and then uses this result to identify a VRS correction spectrum and its coefficients in one final DOAS fit, which is shown in Fig. 8.

AMTD
8, 3423–3469, 2015

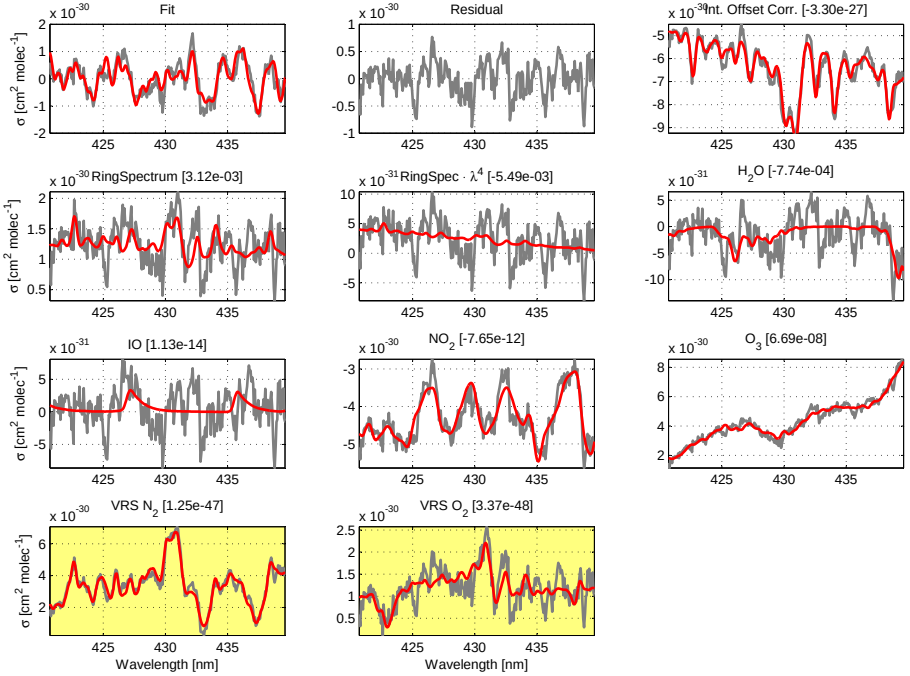

Figure 8. Fit of the Ring-dSCD-correlated residual structure obtained from a linear regression of residual spectra and corresponding dSCDs. The cross-sections for IO, water vapour, NO_2 and O_3 are from the original fits from which the residual spectra were used to solve the system of linear equations. Their coefficients in the fit above are thus dimensionless or could be written as molec cm^{-2} per molec cm^{-2} Ring-dSCD. The absolute magnitude of the VRS spectra in the plot is arbitrary. The VRS spectra are calculated from a solar atlas. The VRRS(N_2/O_2) component is not significant here in the sense that it is not distinguishable from the contribution of the intensity offset correction, which is usually necessary to compensate for instrumental straylight. The spectrum for VRS(N_2) is detected at a size which corresponds to 29 times the fit error, the contribution of VRS(O_2) eight times.

AMTD
8, 3423–3469, 2015

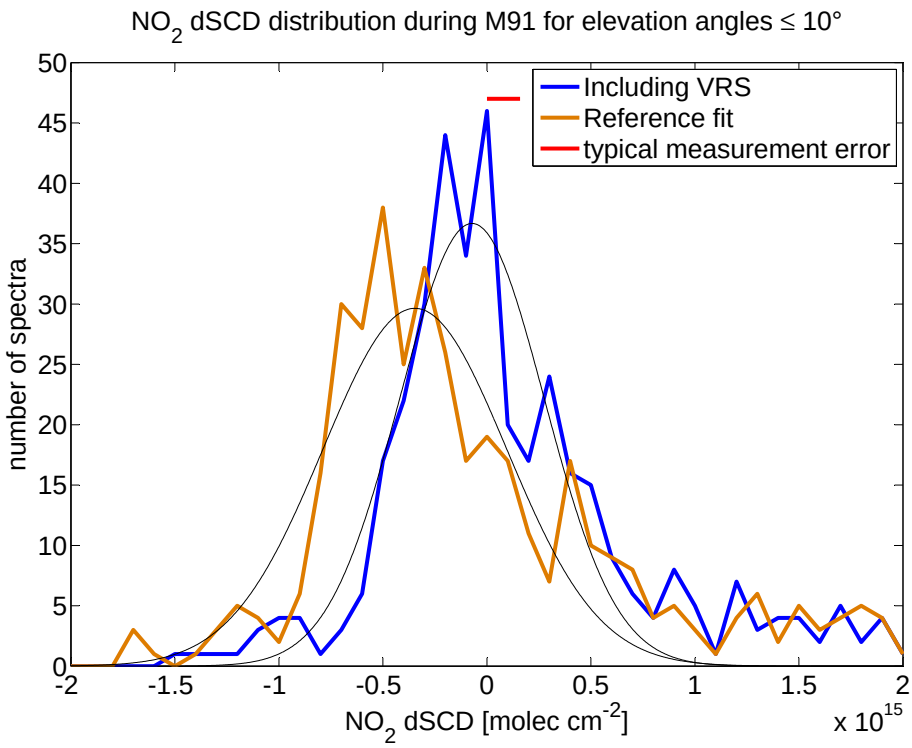

Figure 9. Histogramm of NO_2 dSCDs in the wavelength range from 418–438 nm illustrating the influence of VRS(N_2/O_2) on the spectral retrieval of NO_2. Twice the fit error is shown as a line on the top of the figure. The center of the fitted gaussian curves is shifted from $(-3.5 \pm 0.4) \times 10^{14}$ molec cm^{-2} to $(-0.7 \pm 0.3) \times 10^{14}$ molec cm^{-2}.

AMTD
8, 3423–3469, 2015